Eur. Phys. J. C (2024) 84:1200
https://doi.org/10.1140/epjc/s10052-024-13533-8

THE EUROPEAN PHYSICAL JOURNAL C

Regular Article

Theoretical Physics

Shear-free collapsing compact star in pseudo-flat 5-D spacetime emitting radiation

Ksh. Newton Singh[1,a], **Bidisha Samanta**[2,b], **S. K. Maurya**[3,c], **Farook Rahaman**[2,d], **N. Kamal Singh**[1,e], **Anil K. Aria**[1,f]

[1] Department of Physics, National Defence Academy, Khadakwasla, Pune 411023, India
[2] Department of Mathematics, Jadavpur University, Kolkata 700032, India
[3] Department of Mathematical and Physical Sciences, College of Arts and Sciences, University of Nizwa, Nizwa, Sultanate of Oman

Received: 17 July 2024 / Accepted: 20 October 2024

Abstract A shear-free, collapsing compact object, described by an embedding class I solution and emitting radiation, is presented here. Because of the properties of embedding class I, this four-dimensional interior spacetime can be embedded in pseudo-flat five-dimensional space. Starting with an initially static and shear-free gravitating body through the Karmarkar condition, we have explored the time evolution of the system using the time-dependent Einstein field equations. The interior solution is smoothly matched with the Vaidya outgoing solution across a time-like hypersurface which yields the temporal behaviour of the model. Further, a thorough physical analysis of the thermodynamic variables has been presented spatially and temporally. As the time progresses into the future, the surface compactness factor approaches the Buchdahl limit until it crosses this to proceed with the collapse. Before $2m_\Sigma/r_\Sigma \to 8/9$, the equation of state adjusts itself like a self-immune system to hold the system by increasing Γ_{rc} (i.e. increasing stiffness). All the physical quantities, e.g., density, pressure anisotropy, radiation, luminosity, temperature, are non-singular throughout the interior of the star at a finite time slice. As the time progresses, these quantities point towards a future singularity. Throughout the evolution, the surface density and surface pressure always remain lower than their corresponding central values. Similarly, the causal temperature also always remains higher than the non-causal counterpart throughout the interior as well as during the evolution.

[a] e-mail: ntnphy@gmail.com (corresponding author)
[b] e-mail: samantabidisha@gmail.com
[c] e-mail: sunil@unizwa.edu.om
[d] e-mail: rahaman@iucaa.ernet.in
[e] e-mail: kamalnongmaithem@gmail.com
[f] e-mail: ariaanil@gmail.com

1 Introduction

A collapsing radiating compact star could refer to a scenario in astrophysics where a massive star undergoes gravitational collapse, leading to a compact object such as a neutron star or a black hole. During this collapse, radiation is emitted, often in the form of gamma-ray bursts or other energetic phenomena. This process is of great interest to astronomers and in the field of astrophysics in understanding the life cycles of stars and the physics of extreme environments.

Even in this era of advanced computing power and technologies, solving the Einstein field equations as a whole is still a very difficult task, as these equations are highly nonlinear and coupled. For static cases, exact solutions are possible only once the specific assumptions are made. However, for non-static cases, it remains a challenging task. In non-static cases, the field equations are highly coupled nonlinear partial differential equations. The first analytic solution of the field equations describing collapsing stars (or time-dependent solutions) was presented by Oppenheimer and Snyder [1]. The solution they discovered was simply a model of non-radiating collapse of a spherically symmetric dust distribution with simple initial conditions. In 1943, Vaidya [2] showed that the exterior spacetime surrounding a radiating star is affected by the presence of radiation. The development of this Vaidya solution provided researchers the motivation to model the gravitational collapse of radiating stars. As a result, several physical conditions were brought into the problem, and several researchers proposed various models. In 1964, Minser and Sharp [3] introduced the pressure gradient terms into the equations of motion. In addition, numerous models were proposed that allow outgoing radiation from the collapsing body [4,5] by matching an adiabatic distribution of matter [6]. Afterward, several authors also

Published online: 22 November 2024

discussed radiating solutions assuming perfect fluids [7,8]. The junction conditions were studied for a shear-free isotopic fluid undergoing radial heat flow with outgoing unpolarized radiation [9]. These results were used to study a particular solution of the field equation for the interior of spacetime which can be matched with the exterior solution given by the Vaidya metric, and it was shown that in the infinite past, a static distribution of matter gradually collapses, eventually forming a black hole. The physical process of radiative collapse can be found in the pre (formation) and the post (dying) main sequence (MS) of stars. The collapse originates in an MS star if the hydrogen at the core is exhausted. When MS stars of mass $< 8M_{\odot}$ run out of core hydrogen, they form a degenerate core (due to electron degeneracy) and the collapse will stop, cooling down into white dwarfs. If the mass of the MS stars happens to be more than $8M_{\odot}$, the collapse will continue until a degenerate neutron core is formed. This sudden stop in collapse generates an outward shock-wave which eventually leads to a supernova explosion. It has been shown that dissipative collapse can generate neutrinos [10], which carry away most of the shock-wave energy. If the MS star mass happens to be $> 30M_{\odot}$, it will collapse until a black hole is formed.

Over time, researchers in the fields of astrophysics and cosmology have advanced this field by employing higher-dimensional gravity models, leading to significant discoveries. Recent studies demonstrate many compact star models employing Einstein–Gauss–Bonet gravity, braneworld gravity, and Lovelock gravity. Additionally, the relation between Kaluza–Klein geometry and electromagnetism has been widely studied. However, embedding four-dimensional spacetime into higher dimensions provides an innovative approach for developing various cosmological and astrophysical models. This idea of embedding four-dimensional spacetime into a five-dimensional hypersurface was introduced by Castroa et al. [11], where they embedded four-dimensional spacetime into a five-dimensional braneworld. Another embedding was performed by Karmarkar [12]. Here, four-dimensional spacetime was embedded into five-dimensional Euclidean space, which is known as class I. In this method, the metric coefficients g_{tt} and g_{rr} are linked into an equation, making it easier to solve the field equations. In this paper, we use the Karmarkar condition, which is a necessary and sufficient condition for a spherically symmetric line element to be of class I to derive exact solutions of the Einstein field equations. Ospino and Núñez [13] used the scalar Karmarkar condition to explore all possible class I static solutions by choosing a specific energy density profile. Paliathanasis et al. [14] explored embedding class I solutions using the Lie symmetry method. In addition, Maharaj et al. [15] discussed the Karmarkar embedding condition in several spherically symmetrical metrics admitting Lie symmetries.

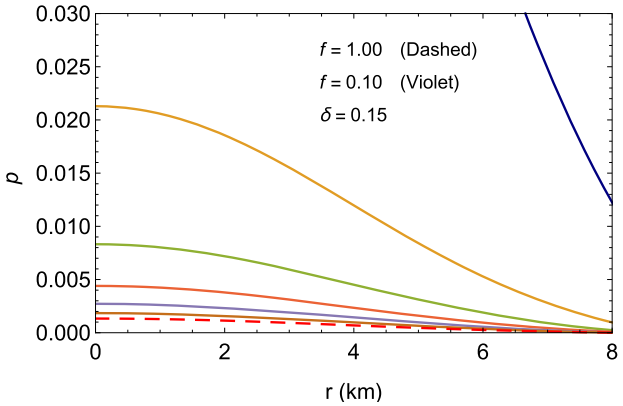

Fig. 1 Variation of radial pressure with radial coordinate r for $c_1 = 0.015$, $C = 0.01$, $c_2 = 0.01$

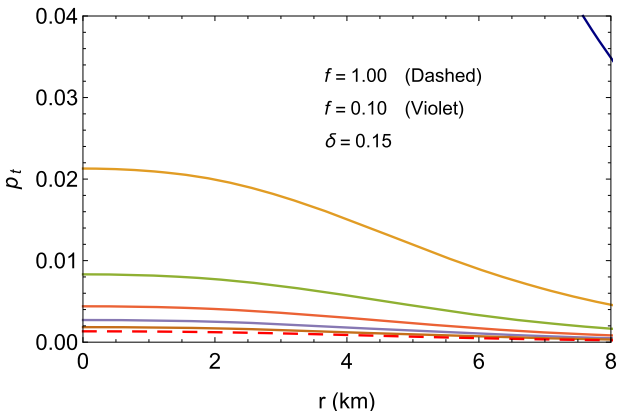

Fig. 2 Variation of transverse pressure with radial coordinate r for the values used in Fig. 1

The paper is organized as follows: In Sect. 2, we consider static Karmarkar spacetime for a spherically symmetric radiating star model using a sheer-free gravitating body and demonstrate the gravitational behaviour of the static solution. In Sect. 3, we consider non-static Karmarkar spacetime and find the solution. In Sects. 4 and 5, a physical analysis of the matter and thermodynamic variables is presented which concludes that our results support recent observations for models in embedding class I.

2 Static Karmarkar spacetime

In order to generate a complete model of dissipative collapse, we assume that the stellar object is initially in a state of static equilibrium. This scenario has been studied by several authors and yielded rich insights into the collapse processes [16–22]. The initial static interior spacetime is given by

$$ds^2 = -A_0(r)^2 dt^2 + B_0(r)^2 dr^2 + r^2\, d\Omega^2, \tag{1}$$

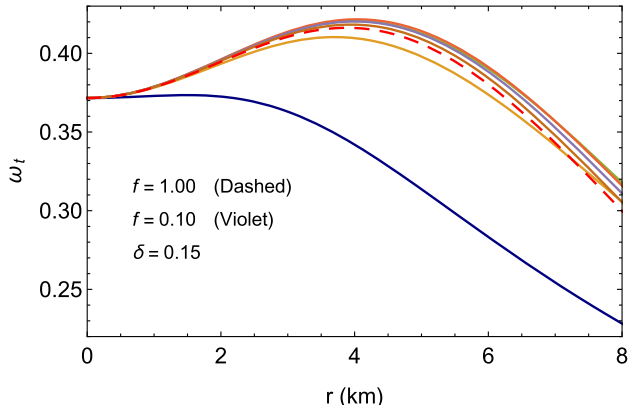

Fig. 3 Variation of p_r and p_t with f for the values used in Fig. 1

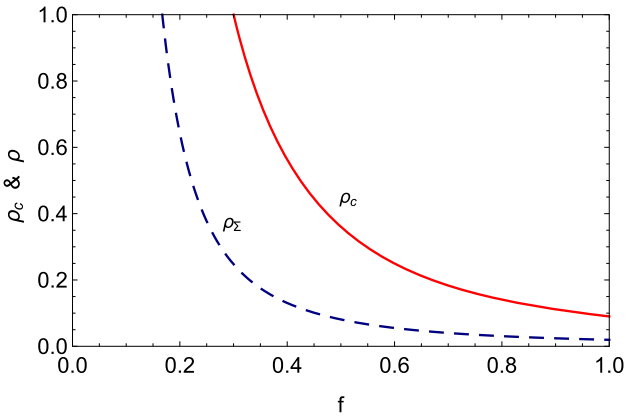

Fig. 5 Variation of density with f for the values used in Fig. 1

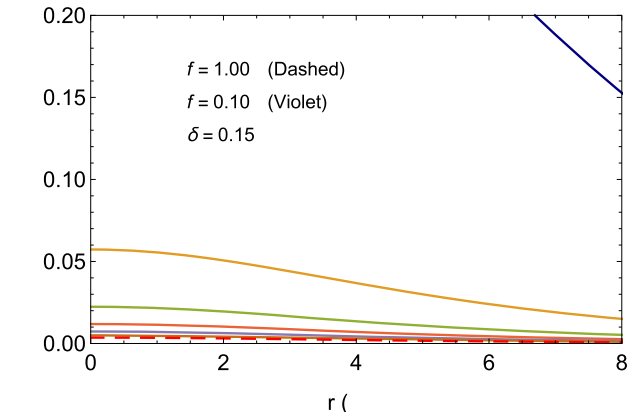

Fig. 4 Variation of density with r for the values used in Fig. 1

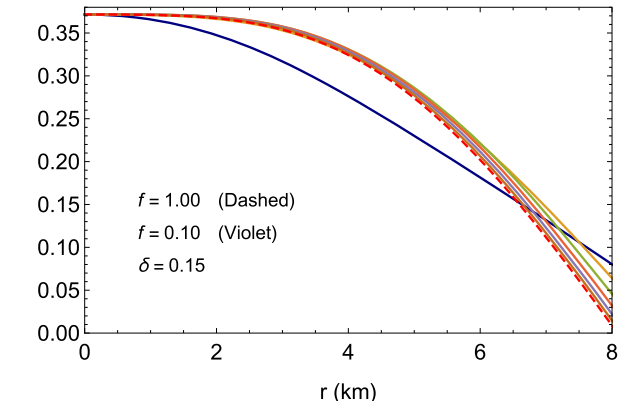

Fig. 6 Variation of $\omega_r = p_r/\rho$ with r for the values used in Fig. 1

where $\mathrm{d}\Omega^2 = \mathrm{d}\theta^2 + \sin^2\theta\,\mathrm{d}\phi^2$, and the functions (A_0, B_0) are only dependent on r. Assuming the static energy–momentum tensor as

$$T_{\mu\nu} = (\rho_s + p_{Ts})u_\mu u_\nu + p_{Ts}\,g_{\mu\nu} + (p_{Rs} - p_{Ts})\chi_\mu\chi_\nu, \quad (2)$$

provided ρ_s, p_{Rs}, and p_{Ts} are the energy density, radial pressure, and tangential pressure, respectively, for comoving coordinates, we can write

$$u^\mu = A^{-1}\delta^\mu_0, \quad \chi^\mu = B^{-1}\delta^\mu_1\,, \quad (3)$$

where u^μ is the time-like four-velocity vector and χ^μ is the unit space-like vector.

The Einstein field equations take the form

$$\rho_s = -\frac{1}{{B_0}^2}\left[2\left(\frac{{B_0}'}{B_0}\right)' + \left(\frac{{B_0}'}{B_0}\right)^2 + \frac{4}{r}\frac{{B_0}'}{B_0}\right], \quad (4)$$

$$p_{Rs} = \frac{1}{{B_0}^2}\left[\left(\frac{{B_0}'}{B_0}\right)^2 + 2\frac{{A_0}'}{A_0}\frac{{B_0}'}{B_0} + \frac{2}{r}\left(\frac{{A_0}'}{A_0} + \frac{{B_0}'}{B_0}\right)\right], \quad (5)$$

$$p_{Ts} = \frac{1}{{B_0}^2}\left[\frac{1}{r}\frac{{A_0}'}{A_0} + \frac{1}{r}\frac{{B_0}'}{{B_0}^3} + \frac{{A_0}''}{A_0} - \left(\frac{{B_0}'}{B_0}\right)^2 + \frac{{B_0}''}{B_0}\right]. \quad (6)$$

The corresponding components of the static Riemann curvature tensor are

$$\mathscr{R}_{1212} = r^2 B_0'^2 - r B_0 B_0' - r^2 B_0 B_0'' \quad (7)$$

$$\mathscr{R}_{1313} = \sin^2\theta\, r^2 B_0'^2 - \sin^2\theta\, r B_0 B_0' - \sin^2\theta\, r^2 B_0 B_0'' \quad (8)$$

$$\mathscr{R}_{1010} = A_0 A_0'' - \frac{A_0 B_0' A_0'}{B_0} \quad (9)$$

$$\mathscr{R}_{2323} = -r^4 B_0'^2 \sin^2\theta - 2r^3 \sin^2\theta\, B_0 B_0' \quad (10)$$

$$\mathscr{R}_{2020} = \frac{r^2 A_0 A_0' B_0'}{B_0} + r A_0 A_0' \quad (11)$$

$$\mathscr{R}_{3020} = \frac{r^2 \sin^2\theta\, A_0 A_0' B_0'}{B_0} + r^2 \sin^2\theta\, A_0 A_0'\,. \quad (12)$$

This can be used in the Karmarkar condition [12]

$$\mathscr{R}_{1010}\mathscr{R}_{2323} = \mathscr{R}_{1212}\mathscr{R}_{3030} - \mathscr{R}_{2102}\mathscr{R}_{3103} \quad (13)$$

along with $\mathscr{R}_{2323} \neq 0$ [23]. Considering the non-zero components of the static Riemann tensor in (13), we obtain

$$\frac{B_0 + 2rB_0'}{r(2B_0 + rB_0')} - \frac{A_0''}{A_0'} + \frac{(B_0 + rB_0')B_0''}{(2B_0 + rB_0')B_0'} = 0, \quad (14)$$

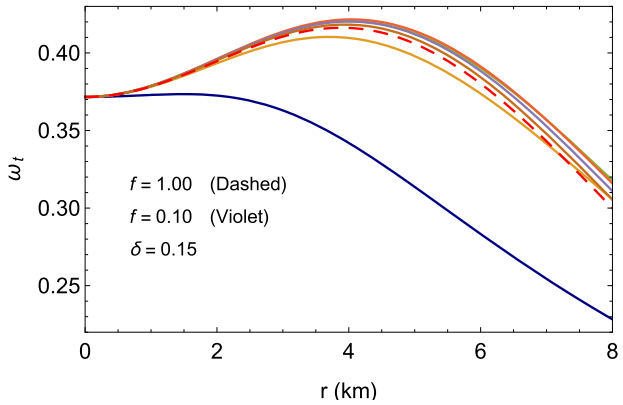

Fig. 7 Variation of $\omega_t = p_t/\rho$ with r for the values used in Fig. 1

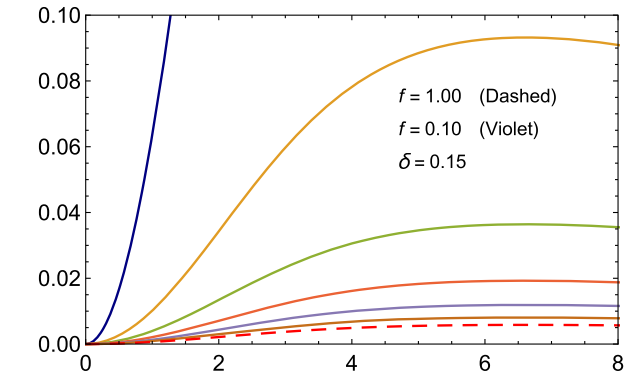

Fig. 8 Variation of anisotropy $\Delta = p_r - p_t$ with r for the values used in Fig. 1

which on integration yields

$$A_0' = C\left[rB_0'(2B_0 + rB_0')\right]^{1/2}. \tag{15}$$

Further integration yields

$$A_0(r) = c_2 + C\int\left[(r^2B_0)'B_0'\right]^{1/2}\mathrm{d}r. \tag{16}$$

Assuming the function $B_0(r)$ as

$$B_0(r) = 1 + c_1r^2, \tag{17}$$

we can integrate (16) to

$$A_0(r) = c_2 + \frac{C}{3\sqrt{c_1}}\left(2c_1r^2 + 1\right)^{3/2}, \tag{18}$$

where c_2 is the constant of integration. Now we have constructed our static solution which will further convert into a non-static solution for collapsing systems.

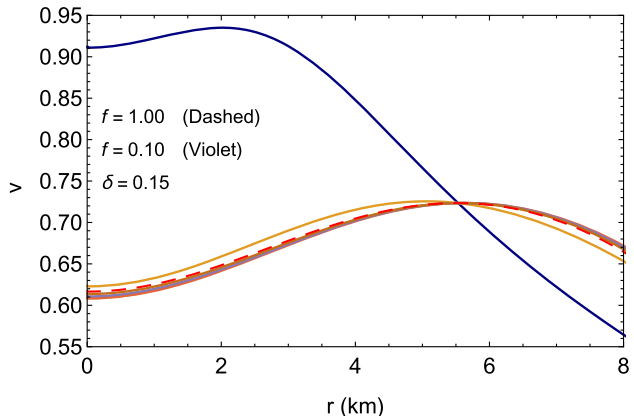

Fig. 9 Variation of radial sound speed with r for the values used in Fig. 1

3 Non-static interior spacetime and boundary conditions

The static interior spacetime (1) can be modified for a radiating star with vanishing shear as

$$\mathrm{d}s_-^2 = -A_0^2(r)\mathrm{d}t^2 + f^2(t)\left[B_0^2(r)\,\mathrm{d}r^2 + r^2\mathrm{d}\Omega^2\right]. \tag{19}$$

It has been found that the density inhomogeneities and dissipation can mimic shear-like effects, which can alter its stability. The shear scalar is defined as [32]

$$Y_{TF} = 16\pi\eta\sigma + \frac{4\pi}{\Re^3}\int_0^R \Re^3\left(D_\Re\rho - 3q\,\frac{D_T\Re}{\Re\,E}\right)d\Re \\ -8\pi(p_r - p_t), \tag{20}$$

which also determines the stability of the shear-free condition. Here, η is the shear viscosity coefficient, σ is the shear viscosity, $D_\Re\,\rho$ is the density inhomogeneity, q is the radial heat flux, $\Re = f(t)\,r$, $D_T = \frac{1}{A_0}\frac{\partial}{\partial t}$, $D_\Re = \frac{1}{\Re'}\frac{\partial}{\partial r}$ and $E = \Re'/B_0$. Now we can see that even in the absence of shear (i.e. $Y_{TF} = 0$), the interlayer friction, the inhomogeneities in density, and dissipation can alter the shear scalar. It is also expected that the shear-free condition during dissipative collapse may hold for a particular epoch of the evolution of the star.

The exterior is governed by the well-known Vaidya metric [4] for a matter-free, null-radiation-filled spacetime given by

$$\mathrm{d}s_+^2 = -\left(1 - \frac{2m(v)}{\mathbb{R}}\right)\mathrm{d}v^2 - 2\mathrm{d}v\,\mathrm{d}\mathbb{R} + \mathbb{R}^2\mathrm{d}\Omega^2, \tag{21}$$

where $m(v)$ represents the mass as perceived by an observer located at infinity. On matching the (19) and (21) at the hypersurface Σ, we obtain

$$A_0(r_\Sigma)\,\mathrm{d}t = \left(1 - \frac{2m}{\mathbb{R}} + 2\frac{\mathrm{d}\mathbb{R}}{\mathrm{d}v}\right)_\Sigma^{1/2}\mathrm{d}v \tag{22}$$

$$r_\Sigma f(t) = \mathbb{R}(v) \tag{23}$$

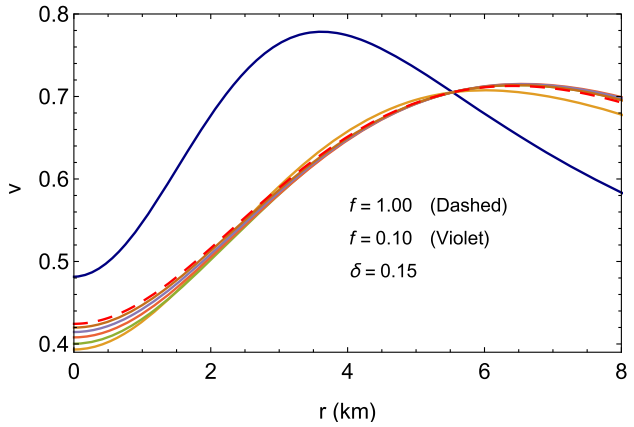

Fig. 10 Variation of transverse sound speed with r for the values used in Fig. 10

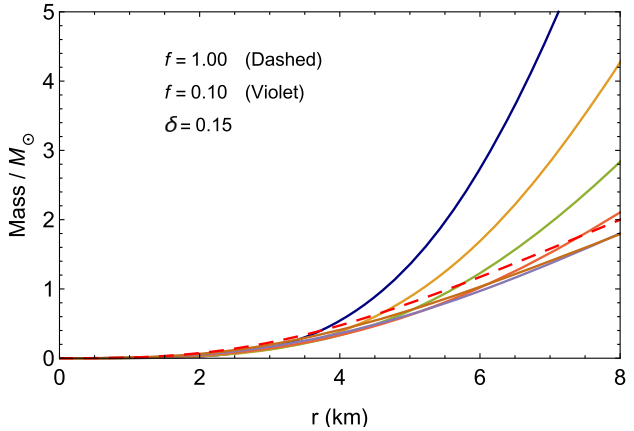

Fig. 11 Variation of mass with r for the values used in Fig. 1

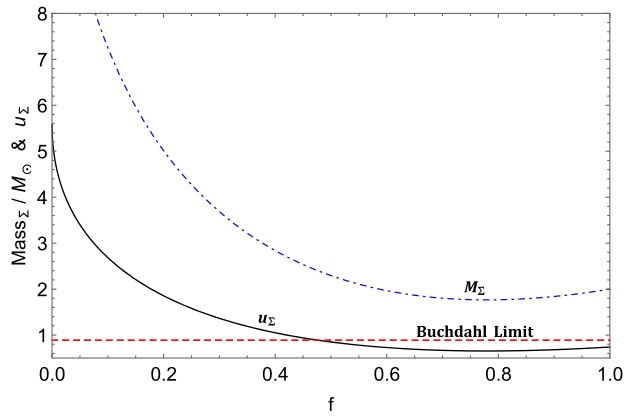

Fig. 12 Variation of compactness parameter with f for the values used in Fig. 1

$$m(v) = m(r_\Sigma, t) = \left[\frac{rf(t)}{2}\left\{\left(\frac{r\dot{f}(t)}{A_0}\right)^2 - \frac{1}{B_0^2} + 1\right\}\right]_\Sigma \tag{24}$$

$$[p_r]_\Sigma = [qB]_\Sigma. \tag{25}$$

In our model, the energy–momentum tensor for the radiating stellar fluid is given by

$$T_{\mu\nu} = (\rho + p_t)u_\mu u_\nu + p_t g_{\mu\nu} + (p_r - p_t)\chi_\mu\chi_\nu + q_\mu u_\nu + q_\nu u_\mu, \tag{26}$$

where ρ is the energy density, p_r and p_t are the radial pressure and tangential pressure, respectively, and q^μ is the heat flow four-vector assumed to flow in the radial direction because of spherical symmetry.

The dynamic Einstein field equations for the line element (19) and energy–momentum tensor (26) are given by

$$\rho = \frac{1}{f^2}\left[\frac{1}{r^2} - \frac{1}{r^2B_0^2} + \frac{2B_0'}{rB_0^3}\right] + \frac{3\dot{f}^2}{A_0^2f^2}, \tag{27}$$

$$p_r = \frac{1}{f^2}\left[-\frac{1}{r^2} + \frac{1}{r^2B_0^2} + \frac{2A_0'}{rA_0B_0^2}\right] - \frac{1}{A_0^2}\left[2\frac{\ddot{f}}{f} + \frac{\dot{f}^2}{f^2}\right], \tag{28}$$

$$p_t = \frac{1}{f^2}\left[\frac{A_0''}{A_0B_0^2} + \frac{A_0'}{rA_0B_0^2} - \frac{B_0'}{rB_0^3} - \frac{A_0'B_0'}{A_0B_0^3}\right] - \frac{1}{A_0^2}\left[2\frac{\ddot{f}}{f} + \frac{\dot{f}^2}{f^2}\right], \tag{29}$$

$$q^1 = -\frac{2A_0'\dot{f}}{8\pi A_0^2B_0^2f^3}, \tag{30}$$

$$\Theta = u^\alpha{}_{;\alpha} = \frac{3\dot{f}}{A_0f} = -\frac{6n(1-\sqrt{f})}{A_0f^{3/2}}. \tag{31}$$

The first three equations further simplify to

$$\rho = \frac{\rho_s}{f^2} + \frac{3\dot{f}^2}{8\pi A_0^2f^2}, \tag{32}$$

$$p_r = \frac{p_{Rs}}{f^2} - \frac{1}{8\pi A_0^2}\left[2\frac{\ddot{f}}{f} + \frac{\dot{f}^2}{f^2}\right], \tag{33}$$

$$p_t = \frac{p_{Ts}}{f^2} - \frac{1}{8\pi A_0^2}\left[2\frac{\ddot{f}}{f} + \frac{\dot{f}^2}{f^2}\right], \tag{34}$$

which contains a static configuration at a particular time slice.

The anisotropy between radial and tangential pressures is defined as

$$\Delta_s(r) = (p_{Rs} - p_{Ts}) = \frac{1}{f^2}\left[-\frac{A_0''}{A_0B_0^2} + \frac{A_0'}{rA_0B_0^2} + \frac{B_0'}{rB_0^3} + \frac{A_0'B_0'}{A_0B_0^3} + \frac{1}{r^2B_0^2} - \frac{1}{r^2}\right], \tag{35}$$

which can also be written as

$$\Delta(r,t) = p_r - p_t = \frac{\Delta_s(r)}{f^2}, \tag{36}$$

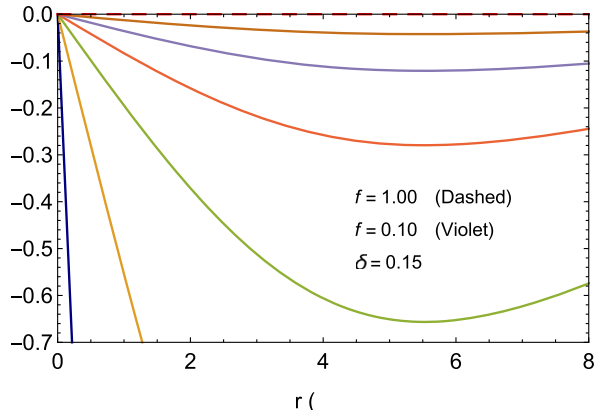

Fig. 13 Variation of rate of collapse with r for the values used in Fig. 1

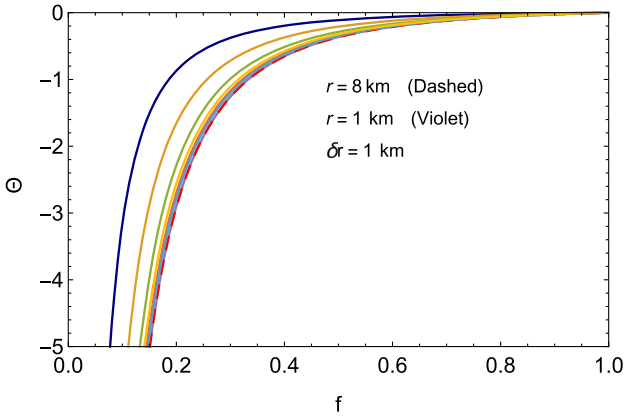

Fig. 14 Variation of rate of collapse with f for the values used in Fig. 1

where Δ_s corresponds to the static configuration.

4 Temporal evolution and physical parameters

Using the Santos [24] junction conditions, one can determine the $f(t)$. Because of the external radiation pressure, radial pressure at the hypersurface is non-vanishing, i.e.,

$$p_{r\Sigma} = (qB)_\Sigma, \tag{37}$$

which leads to a temporal evolution equation

$$2\ddot{f}f + \dot{f}^2 - 2n\dot{f} = 0 \quad \text{with} \quad n = \left(\frac{A_0'}{B_0}\right)_\Sigma. \tag{38}$$

This can be integrated to

$$t = \frac{1}{n}\left[\frac{f}{2} + \sqrt{f} + \log\left(1-\sqrt{f}\right)\right]. \tag{39}$$

This method has been used by various researchers in the case of dissipative gravitational collapse [25–29].

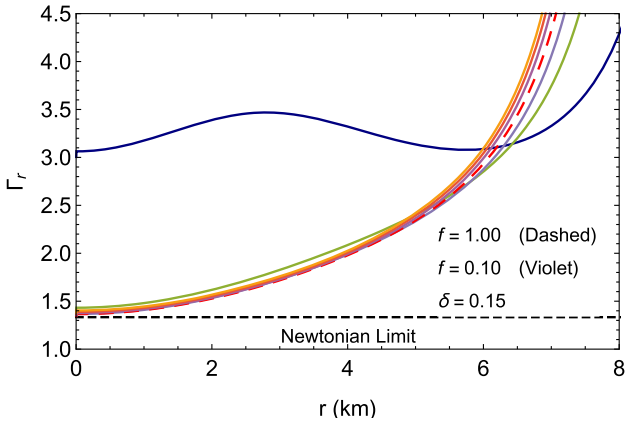

Fig. 15 Variation of adiabatic index with r for the values used in Fig. 1

Now the thermodynamic quantities through the field equations take the form

$$\rho = \frac{\rho_s}{f^2} + \frac{3n^2(1-\sqrt{f})^2}{2\pi A_0^2 f^3}, \tag{40}$$

$$p_r = \frac{p_{Rs}}{f^2} + \frac{n^2(1-\sqrt{f})}{2\pi A_0^2\sqrt{f^5}}, \tag{41}$$

$$p_t = \frac{p_{Ts}}{f^2} + \frac{n^2(1-\sqrt{f})}{2\pi A_0^2\sqrt{f^5}}, \tag{42}$$

$$q^1 = \frac{18c_1^2C^2\left(1-\sqrt{f}\right)r^2\left(2c_1r^2+1\right)^2}{\pi f^{7/2}\left(c_1r^2+1\right)^3} \times\left[4c_1^2Cr^4+4c_1Cr^2+3c_2\sqrt{c_1\left(2c_1r^2+1\right)}+C\right]^{-2} \tag{43}$$

$$L_\Sigma = 4\pi q^1\mathbb{R}^2 = \frac{72c_1^2C^2\left(1-\sqrt{f}\right)r_\Sigma^4\left(2c_1r_\Sigma^2+1\right)^2}{f^{3/2}\left(c_1r_\Sigma^2+1\right)^3} \times\left[4c_1^2Cr_\Sigma^4+4c_1Cr_\Sigma^2+3c_2\sqrt{c_1\left(2c_1r_\Sigma^2+1\right)}+C\right]^{-2} \tag{44}$$

$$\Theta = -\frac{12r\sqrt{c_1}\,C\left(1-\sqrt{f}\right)\sqrt{2c_1r^2+1}}{f^{3/2}\left(c_1r^2+1\right)\left[c_2+\frac{C}{3\sqrt{c_1}}\left(2c_1r^2+1\right)^{3/2}\right]}, \tag{45}$$

where the non-dynamic quantities are given by

$$\rho_s = \frac{c_1\left(c_1^2r^4+3c_1r^2+6\right)}{\left(c_1r^2+1\right)^3} \tag{46}$$

$$p_{Rs} = \frac{c_1\left(c_1r^2+1\right)^{-2}}{4c_1^2Cr^4+4c_1Cr^2+3c_2\sqrt{c_1\left(2c_1r^2+1\right)}+C} \times\left[10C-4c_1^3Cr^6-12c_1^2Cr^4+3c_1r^2\left(5d-c_2\sqrt{c_1\left(2c_1r^2+1\right)}\right)-6c_2\sqrt{c_1\left(2c_1r^2+1\right)}\right] \tag{47}$$

$$p_{Ts} = \frac{2c_1^2Cr^4+14c_1Cr^2-3c_2\sqrt{c_1\left(2c_1r^2+1\right)}+5C}{4c_1^2Cr^4+4c_1Cr^2+3c_2\sqrt{c_1\left(2c_1r^2+1\right)}+C}$$

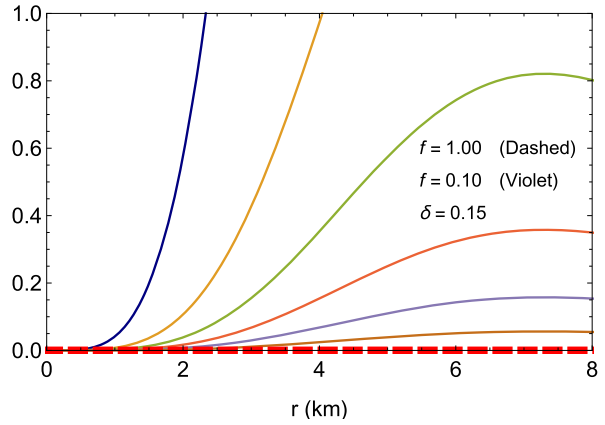

Fig. 16 Variation of surface luminosity with r for the values used in Fig. 1

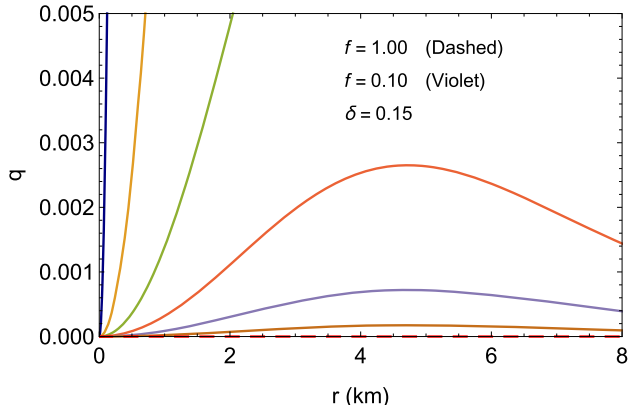

Fig. 17 Variation of heat flux with r for the values used in Fig. 1

$$\times \frac{2c_1}{\left(c_1 r^2+1\right)^3}. \tag{48}$$

The variations of these parameters are given in Figs. 1, 2, 3, 4, and 5. The equation of state parameters, i.e. $\omega_t = p_{Ts}$ and $\omega_r = p_{Rs}$ variations, are shown in Figs. 6 and 7. The variation of the pressure anisotropy is also shown in Fig. 8, where one can see that the anisotropy is increasing with future time parameter f. The causality of the system is also satisfied for a finite time future (see Fig. 9 and 10); however, it tends towards violating the causality in far future time (collapsing stage). The mass function and the compactness factor variations with r can be seen in Figs. 11 and 12, where both tend to increase toward future time. The compactness factor crosses the Buchdahl limit from around $f = 0.4$, i.e., a finite future time slice, implying that the system will proceed to a gravitational collapse at $f = 0.4$. The variations of collapse rate, adiabatic index, surface luminosity, and heat flux are shown in Figs. 13, 14, 15, 16, 17, and 18. Many authors have also presented shear-free radiating collapse [30–43]. Numerous static solutions have also been explored by several authors [44–49].

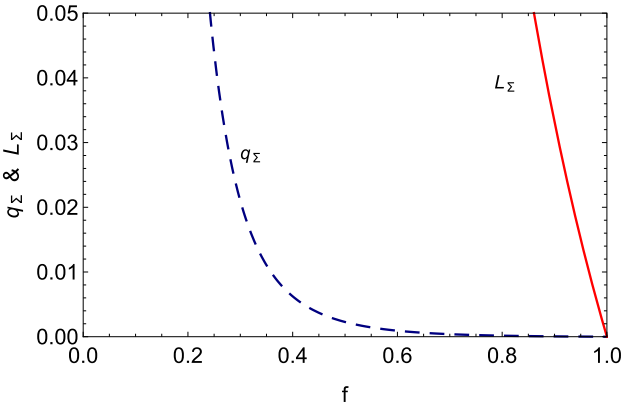

Fig. 18 Variation of surface luminosity and heat flux with f for the values used in Fig. 1

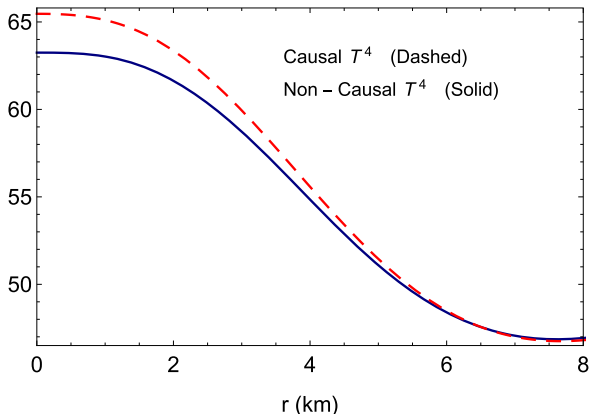

Fig. 19 Variation of temperature with r for the values used in Fig. 1

5 Heat transport equation and thermodynamics

The use of extended irreversible thermodynamics has been well motivated and extensively used to determine the causal temperature profiles of radiating stars [30]. The causal transport equation for the line element (19) is given by

$$\tau\ \partial_t(qB) + A_0 q\ B = -\frac{\kappa}{B}\ \partial_r(A_0\ T) \quad \text{where}$$
$$B \equiv f(t)\ B_0(r), \tag{49}$$

where

$$\kappa = \gamma T^3 \tau_c, \qquad \tau_c = \left(\frac{\psi}{\gamma}\right) T^{-\sigma}, \qquad \tau = \left(\frac{\beta\gamma}{\psi}\right)\tau_c, \tag{50}$$

where κ is the thermal conductivity, τ_c is the mean collision time of massive–massless particles, and the relaxation time is τ. Now the causal heat transport equation (49) becomes

$$\beta\ \partial_t(qB)\ T^{-\sigma} + A_0(qB) = -\psi\ \frac{T^{3-\sigma}}{B}\ \partial_r(A_0 T). \tag{51}$$

The integration of (51) for constant and variable τ was proposed by Govinder and Govender [43].

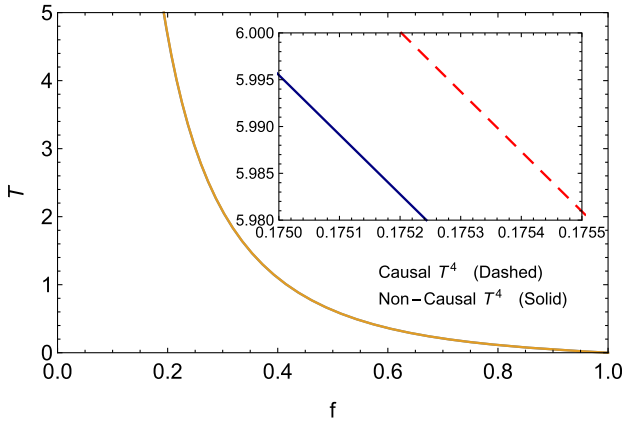

Fig. 20 Variation of temperature with f for the values used in Fig. 1

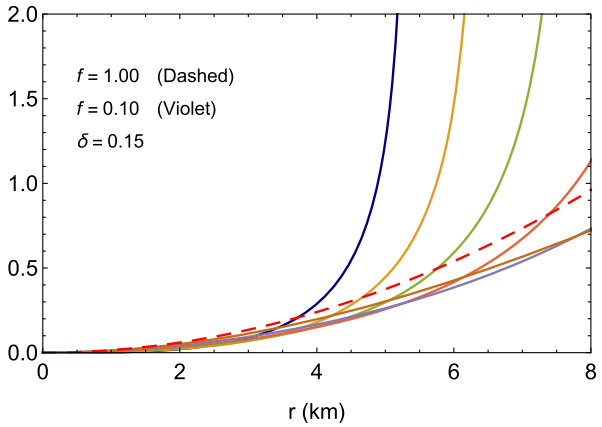

Fig. 21 Variation of surface redshift with r for the values used in Fig. 1

For mean collision time $\sigma = 0$, the solution of (51) is

$$(AT)^4 = -\frac{4}{\psi}\left[\beta\int A^3 B\,\partial_t(qB)\,\mathrm{d}r + \int A^4 q\,B^2\mathrm{d}r\right] + g(t), \tag{52}$$

where $g(t)$ is the function of integration which can be fixed by the surface temperature. The effective surface temperature can be defined as

$$(T^4)_\Sigma = \frac{1}{r^2B^2}\bigg|_\Sigma \frac{L_\infty}{4\pi\delta}, \tag{53}$$

where $\delta > 0$, and L_∞ is the total luminosity at infinity.

The solutions of (52) for causal and non-causal temperature for mean collision time are respectively

$$T_c^4 = g(t) + \frac{1}{1890\pi c_1 f^3\psi\left[d\left(2c_1r^2+1\right)^{3/2} + 3\sqrt{c_1}c_2\right]^4} \times\Bigg[\Bigg\{\frac{5040\beta\sqrt{c_1}d(4\sqrt{f}-5)\mu_1(r)}{c_1r^2+1} - f^{3/2}\Big(315\sqrt{c_1}c_2 d\,\mu_3(r) + 15120c_1c_2^2\mu_4(r) + 16d^2\mu_2(r)\Big)\Bigg\}d^2\left(1-\sqrt{f}\right)\Bigg] \tag{54}$$

$$T_{nc}^4 = g(t) + \frac{1}{70\pi f^{3/2}\psi\left[3c_2\sqrt{c_1} + d(2c_1r^2+1)^{3/2}\right]^4} \times\Bigg[\sqrt{c_1}d^2\left(\sqrt{f}-1\right)\Big\{315c_2d\sqrt{c_1}\,\zeta_2(r) + 15120c_1c_2^2 \times\left(\sqrt{c_1}r(2c_1r^2-3) + 3\tan^{-1}(\sqrt{c_1}r)\right) + \zeta_1(r)\Big\}\Bigg], \tag{55}$$

where

$$\mu_1(r) = d\Big[8c_1^4r^8 + 2c_1^3r^6 + 12c_1^2r^4 + 18c_1r^2 - 21(c_1r^2+1) \times\log\left(c_1r^2+1\right) - 3\Big] + 3\sqrt{c_1}c_2\Big[24(c_1r^2+1) \times\tan^{-1}\left(\sqrt{2c_1r^2+1}\right) + \sqrt{2c_1r^2+1} \times(4c_1^2r^4 - 12c_1r^2 - 19)\Big] \tag{56}$$

$$\mu_2(r) = \sqrt{c_1}r\left(560c_1^4r^8 + 720c_1^3r^6 + 504c_1^2r^4 + 315\right) - 315\tan^{-1}\left(\sqrt{c_1}r\right) \tag{57}$$

$$\mu_3(r) = 42\sqrt{c_1}r\sqrt{2c_1r^2+1} + 24\log\Big(3c_1r^2 + 1 + 2\sqrt{c_1}r \times\sqrt{2c_1r^2+1}\Big) - 24\log\Big(3c_1r^2 - 2\sqrt{c_1}r\sqrt{2c_1r^2+1} + 1\Big) + 64c_1^{5/2}r^5\sqrt{2c_1r^2+1} + 8c_1^{3/2}r^3\sqrt{2c_1r^2+1} - 69\sqrt{2}\sinh^{-1}\left(\sqrt{2c_1}r\right) \tag{58}$$

$$\mu_4(r) = \sqrt{c_1}r\left(2c_1r^2-3\right) + 3\tan^{-1}\left(\sqrt{c_1}r\right) \tag{59}$$

$$\zeta_1(r) = 16d^2\Big[\sqrt{c_1}r\left(560c_1^4r^8 + 720c_1^3r^6 + 504c_1^2r^4 + 315\right) - 315\tan^{-1}\left(\sqrt{c_1}r\right)\Big] \tag{60}$$

$$\zeta_2(r) = 42\sqrt{c_1}r\sqrt{2c_1r^2+1} + 24\log\left(3c_1r^2 + 1 + 2\sqrt{c_1}r \times\sqrt{2c_1r^2+1}\right) - 24\log\left(3c_1r^2 + 1 - 2\sqrt{c_1}r \times\sqrt{2c_1r^2+1}\right) + 64c_1^{5/2}r^5\sqrt{2c_1r^2+1} + 8c_1^{3/2}r^3 \times\sqrt{2c_1r^2+1} - 69\sqrt{2}\sinh^{-1}\left(\sqrt{2}\sqrt{c_1}r\right). \tag{61}$$

The temporal and spatial behaviour of the causal and non-causal temperatures is plotted in Figs. 19 and 20, which shows that the causal temperature is higher than the non-causal temperature at the center of the compact star, while they are the same at the surface. However, throughout the evolution time in the future, the causal temperature is also greater than the non-causal temperature. As the compact object evolves, the star becomes more compact and hence the surface redshift increases over time, eventually exploding in the far future when the singularity is formed (Fig. 21).

6 Results and final comments

We have presented a static compact model which in the near future will initiate a shear-free radiative collapse to form a singularity. The initial static solution was described by $A_0(r)$ and $B_0(r)$ metric potentials, while the future evolution was described by a $f(t)$. To simplify the model, we have

assumed that the $A_0(r)$ metric function was static throughout the evolution while the g_{11} metric function was evolving as $f(t)B_0(r)$. As the outer spacetime was filled with radiation, the exterior spacetime was taken to be Vaidya's metric, which was smoothly connected with the interior at the boundary of the hypersurface Σ. During the evolution of the radiative collapse, the pressures, anisotropy, and density are finite throughout the interior in the finite near future (Figs. 1, 2, 4, 8). These quantities also increase over time until they explode in the far future $f \to 0$. However, throughout the entire evolution, the central pressure and density remain higher than the corresponding surface values (Figs. 3, 5). An important observation can be made from the equation of state parameters $\omega_i = p_i/\rho$, i.e., during the entire evolution time, the matter at the interior never becomes exotic (Figs. 6, 7). The speed of sound tends to violate the causality when the formation of a singularity started in the far future (Figs. 9, 10). As the stellar system starts compressing in the process of collapsing, the compactness factor $u_\Sigma = 2m_\Sigma/r_\Sigma$ approaches the Buchdahl limit 8/9. At a finite future time of $f \approx 0.479$, the compactness factor crosses the Buchdahl limit, resulting in the initiation of the radiative collapse. The collapsing scalar also vanishes at the present moment $f = 1$ (see Fig. 13) but increases if we forward to the future time $f \to 0$. One can also observe that the rate of surface collapse θ_Σ increases with the surface radius (see Fig. 14). The static configuration at $f = 1$ has a central adiabatic index of 1.4, which is above the Bondi limit of 1.33, and hence the system was non-collapsing. Because of external processes such as accretion, matter accumulates from the surrounding to increase the density, pressure, and anisotropy, as well as the mass. The system also reacted as a self-immune system to hold the static configuration by increasing the adiabatic index ($\Gamma_{rc} \approx 3$ at $f = 0.1$, see Fig. 15), to increase the stiffness of the equation of state. However, the violation of the Buchdahl limit causes the system to collapse at around $f = 0.479$. As the collapse continues into the future, radiation is emitted at the exterior, and the luminosity and heat flux increase (see Figs. 16, 17, 18). Due to the presence of heat radiation, the thermodynamics in the static condition will be completely different from the non-static condition. The new thermodynamics can be dealt with by the heat transport equation for which one can trace the temperature profile (see Figs. 19, 20). Throughout the evolution, the causal temperature is always higher than the non-causal temperature. At the end, the evolution of surface redshift is shown in Fig. 21.

Acknowledgements KNS and FR would like to thank the authorities of the Inter-University Centre for Astronomy and Astrophysics, Pune, India for providing the research facilities. FR is also thankful to SERB, DST, Govt. of India for financial support.

Funding The authors declare that they have no known competing financial interests.

Data Availability Statement This manuscript has no associated data. [Authors' comment: No data was used for the research described in the article.]

Code Availability Statement This manuscript has no associated code/software. [Authors' comment: Code/Software sharing not applicable to this article as no code/software was generated or analysed during the current study.]

Funded by SCOAP[3].

References

1. J.R. Oppenheimer, H. Snyder, Phys. Rev. **55**, 455 (1939)
2. P.C. Vaidya, Curr. Sci. **12**, 183 (1943)
3. C.W. Misner, D.H. Sharp, Phys. Rev. **136**, B571 (1964)
4. P.C. Vaidya, Proc. Indian Acad. Sci. A **33**, 264 (1951)
5. P.C. Vaidya, Astrophys. J. **144**, 943 (1966)
6. C.W. Misner, D.H. Sharp, Phys. Lett. **15**, 279 (1965)
7. N. Chakravarty, S.B. Dutta Choudhury, A. Banerjee, Aust. J. Phys. **29**, 113 (1976)
8. A. Banerjee, S. Banerji, Acta Phys. Pol. B **7**, 389 (1976)
9. N.O. Santos, Mon. Not. R. Astron. Soc. **216**, 403–410 (1985)
10. E.N. Glass, J. Math. Phys. (N.Y.) **31**, 1974 (1990)
11. L.B. Castroa, M.D. Alloy, D.P. Menezes, JCAP **08**, 047 (2014)
12. K.R. Karmarkar, Proc. Indian. Acad. Sci. A **27**, 56 (1948)
13. J. Ospino, L.A. Núñez, Eur. Phys. J. C **80**, 166 (2020)
14. A. Paliathanasis, R.S. Bogadi, M. Govender, Eur. Phys. J. C **82**, 987 (2022)
15. S.D. Maharaj, N. Naidoo, G. Ameryc, K.S. Govinder, Eur. Phys. J. C **83**, 333 (2023)
16. R. Sharma, R. Tikekar, Gen. Relativ. Gravit. **44**, 2503 (2012)
17. R. Sharma, R. Tikekar, Pramana J. Phys. **79**, 501 (2012)
18. R. Sharma, S. Das, J. Gravit. **659605**, 1 (2013)
19. N. Naidu, M. Govender, Int. J. Mod. Phys. D **25**, 1650092 (2016)
20. M. Govender, R. Bogadi, R. Sharma, S. Das, Astrophys. Space Sci. **361**, 33 (2016)
21. M. Govender et al., Int. J. Mod. Phys. D **25**, 1650037 (2016)
22. E.N. Glass, Phys. Lett. A **867**, 351 (1981)
23. S.N. Pandey, S.P. Sharma, Gen. Relativ. Gravit. **14**, 113 (1981)
24. N.O. Santos, MNRAS **216**, 403 (1985)
25. W.B. Bonnor et al., Phys. Rep. **181**, 269 (1989)
26. R. Sharma, R. Tikekar, Gen. Relativ. Gravit. **44**, 2503 (2012)
27. N.F. Naidu, M. Govender, Int. J. Mod. Phys. D **25**, 1650092 (2016)
28. M. Govender et al., Mod. Phys. Lett. A **35**, 2050164 (2020)
29. N.F. Naidu, M. Govender, K.S. Govinder, Int. J. Mod. Phys. D **15**, 1053 (2006)
30. S.D. Maharaj, M. Govender, Pramana J. Phys. **54**, 715 (2000)
31. L. Herrera, G. Le Denmat, N.O. Santos, Phys. Rev. D **79**, 087505 (2009)

32. L. Herrera, A. Di Prisco, N.O. Santos, Gen. Relativ. Gravit. **42**, 1585 (2010)
33. L. Herrera, G. Le Denmat, N.O. Santos, Gen. Relativ. Gravit. **44**, 1143 (2012)
34. M. Govender, S.D. Maharaj, R. Maartens, Class. Quantum Gravity **15**, 323 (1998)
35. M. Govender, R. Maartens, S.D. Maharaj, Mon. Not. R. Astron. Soc. **310**, 557 (1999)
36. R. Maartens, M. Govender, S.D. Maharaj, Gen. Relativ. Gravit. **31**, 815 (1999)
37. S.D. Maharaj, M. Govender, Int. J. Mod. Phys. D **14**, 667 (2005)
38. A.M. Msomi, K.S. Govinder, S.D. Maharaj, Int. J. Theor. Phys. **51**, 1290 (2012)
39. G.Z. Abebe, K.S. Govinder, S.D. Maharaj, Int. J. Theor. Phys. **52**, 3244 (2013)
40. G.Z. Abebe, S.D. Maharaj, K.S. Govinder, Gen. Relativ. Gravit. **46**, 1650 (2014)
41. A. Banerjee, S. Chatterjee, N. Dadhich, Mod. Phys. Lett. A **17**, 2335 (2002)
42. N.F. Naidu, M. Govender, S. Thirukkanesh, S.D. Maharaj, Gen. Relativ. Gravit. **49**, 95 (2017)
43. K.S. Govinder, M. Govender, Phys. Lett. A **283**, 71 (2001)
44. K.N. Singh, N. Pant, Eur. Phys. J. C **76**, 524 (2016)
45. K.N. Singh, N. Pant, M. Govender, Eur. Phys. J. C **77**, 100 (2017)
46. K.N. Singh et al., Chin. Phys. C **41**, 015103 (2017)
47. S.K. Maurya et al., Eur. Phys. J. C **75**, 389 (2015)
48. S.K. Maurya et al., Eur. Phys. J. A **52**, 191 (2016)
49. M. Kohler, K.L. Chao, Z. Naturforchg **20**, 1537 (1965)